Journal of Water Process Engineering 85 (2026) 109745

Contents lists available at ScienceDirect

Journal of Water Process Engineering

journal homepage: www.elsevier.com/locate/jwpe

Biopolymer-mediated fabrication of zirconyl ferrite bionanocomposites: A sustainable approach for photocatalytic removal of malachite green

Akshara Bassi [a], Parvathalu Kalakonda [b], Mohammad Aslam [c,1], Imran Hasan [d,*,1]

[a] University Centre for Research and Development, Chandigarh University, Mohali, 140413, Punjab, Mohali, India
[b] Department of Physics, Smart Nano Materials Research Laboratory, Government City PG College Autonomous, Osmania University, Hyderabad, Telangana, 50002, India
[c] School of Chemical Engineering, Yeungnam University, Gyeongsan, 38541, Republic of Korea
[d] Department of Chemistry, College of Science, King Saud University, P.O. Box 2455, Riyadh, 11451, Saudi Arabia

ARTICLE INFO

Editor: Gamze Varank

Keywords:
Bionanocomposites
Malachite green
Guar-gum
Photocatalytic degradation
Zirconyl ferrite

ABSTRACT

The synthesis of zirconyl ferrite ($ZrFe_2O_4$) nanoparticles (NPs) immobilized within a guar-gum (GG) biopolymer matrix using a combination of the coprecipitation method and sol-gel method, resulting in the successful formation of GG@ZrFe bionanocomposite (BNC) is reported in this work. The synthesized composite was thoroughly examined using analytical methods, namely FTIR, XRD, SEM-EDX, TEM, XPS, VSM, UV–Vis spectroscopy, PL spectroscopy, and Zeta potential measurements. The optical studies revealed a direct band gap of 1.23 eV, which shows a strong potential as visible-light driven photocatalyst. TEM analysis reveals a homogenous distribution of NPs with an average particle size of 11.20 nm. The photocatalytic activity of GG@ZrFe BNC was investigated using malachite green (MG) dye under visible light irradiation. The composite shows remarkable activity, achieving 99.79% degradation of 40 mg L^{-1} MG solution at pH 8 within 30 min of visible light exposure. According to kinetics analysis, the degradation process was a pseudo-first order, with a rate constant (k_1) of 0.09 min^{-1}, and a minimum half-life of 7.7 min at 40 mg L^{-1} accompanied by correlation coefficient (R^2) of 0.99. The reactive species trapping experiments revealed that superoxide radicals ($^{\bullet}O_2^-$) played the predominant role in the mechanism of MG degradation. Furthermore, the GG@ZrFe BNC shows outstanding reusability, maintaining high photocatalytic efficiency for five consecutive cycles. These results demonstrate the GG@ZrFe BNC as highly efficient, recyclable photocatalyst with strong potential for the removal of organic pollutants such as malachite green from wastewater.

1. Introduction

Dyes, commonly used in the textile industries, pose a serious threat to the aquatic ecosystems owing to their toxic nature and capacity to cause discoloration. These organic pollutants are toxic to aquatic life and destroy the natural balance of water bodies [1,2]. Out of these, malachite green dye (MG), is a basic cationic dye from the triphenylmethane family, widely used in food and textiles industries for colouring materials such as cotton, paper, silk, leather, and jute [3,4]. However, MG is extremely toxic due to its complex structure, non-biodegradability, and other negative health impacts [5,6]. Such regulatory bodies as the US Food and drug administration (FDA) and the European Union have prohibited its use. MG is known to be highly carcinogenic, mutagenic, and genotoxic, posing significant risks to both human and aquatic life [7–9]. It can cause severe damage to multi organ systems, including the reproductive and immune system [10,11]. Additionally, the presence of MG in wastewater significantly raises environmental parameters such as biochemical oxygen demand (BOD > 80 mgL^{-1}), chemical oxygen demand (COD > 150 mgL^{-1}) and total organic carbon (TOC > 2900 mgL^{-1}), reducing water quality and usability [12]. To avoid the degradation of the environment and safeguard human health, it is important to remove these hazardous dyes from the wastewater [13,14]. The extent and prolonged effects of MG on the ecosystems and human health require the implementation of the effective treatment methods [15,16].

Wastewater dye removal processes include wet oxidation,

* Corresponding author at: Department of Chemistry, College of Science, King Saud University, P.O. Box 2455, Riyadh, 11451, Saudi Arabia
E-mail addresses: bassiakshara@gmail.com (A. Bassi), parvathalu.k@gmail.com (P. Kalakonda), mohammadaslam13@gmail.com (M. Aslam), iabdulateef@ksu.edu.sa (I. Hasan).
[1] Equal contribution.

https://doi.org/10.1016/j.jwpe.2026.109745
Received 2 October 2025; Received in revised form 11 February 2026; Accepted 14 February 2026
Available online 26 February 2026

adsorption, coagulation, flocculation, and ion exchange are commonly used but commonly have limitations like high maintenance, extensive chemical requirements, and high operational costs [17–19]. Conversely, photocatalysis proves to be an eco-friendly alternative having advantages, including cost-effectiveness, high efficiency, and high chemical stability, making it a sustainable and economical approach [20]. When exposed to light, a semiconductor-based photocatalyst generates electron-hole pairs, that give rise to reactive species, such as hydroxyl and superoxide radicals, that drive the degradation of organic pollutants under UV–Vis light irradiation [20,21].

The nanocrystal magnetic spinel ferrites with general formula (MFe_2O_4; M = Ni^{2+}, Zn^{2+}, Mn^{2+} or Zr^{2+}) have remarkable properties, such as tuneable shape and size, high surface area, purity, narrow band gap, and high catalytic, magnetic, and chemical stability [22,23]. These ferrites-based materials are emerging as promising semiconductors photocatalyst owing to their affordability and non-toxic nature [24]. Among these, zirconyl ferrite ($ZrFe_2O_4$) stands out for its distinctive properties, as narrow band gap, high surface area, small particle size, thermal stability, and superior electrical and optical characteristics [25]. However, $ZrFe_2O_4$ NPs tend to aggregate, which promotes electron-hole recombination, thereby limiting their photocatalytic performance [26]. To address this challenge, this study explores chemical surface modification through surface grafting with biopolymer chains.

Biopolymers derived mainly from proteins and carbohydrates containing abundant hydroxy and carboxyl groups, promote the green route for the NPs synthesis by forming a supportive matrix that acts as both stabilizer and crosslinker [27]. Guar-gum (GG) is natural polysaccharide extracted from the seeds of Cyamopsis tetragonolobus of Leguminosae family, is renowned for its water solubility, non-ionic nature, and hydrophilic properties [28,29]. GG has a galactomannan structure, characterized β-(1–4)-linked mannopyranose backbone and α-(1, 6)-linked galactopyranose side chain [30,31]. GG is valued for its biocompatibility, biodegradability, cost effectiveness, accessibility, non-toxic nature, and eco-friendliness, along with its ability to chelate metal ions [32,33]. These attributes make it versatile across diverse fields, and notably, GG's ability to cap and stabilize semiconductor materials is particularly significant. Extensively used in industries including pharmaceutical, food, textile, cosmetic, paint, oil, and explosive, GG demonstrates exceptional functionality [34,35]. The presence of hydrogen bonding in its molecular structure facilitates intermolecular chain interactions, further enhancing its applicability and performance in various domains [36].

Recent research in biopolymer-ferrite photocatalysis has focused on combining natural polymers with ferrite-based semiconductors to enhance dye degradation performance through improved charge separation, adsorption, and sustainability. For example, $MnFe_2O_4$/GO/chitosan nanocomposites demonstrated near-complete removal of Brilliant Blue FCF and Reactive Red 198 dyes under both UV and sunlight, attributed to synergistic effects between ferrite, graphene oxide, and the biopolymer that boost adsorption and reactive oxygen species generation [37]. Another study ZnO–Fe_2O_3 nanoparticles embedded in a guar-gum–carboxymethyl cellulose biopolymer matrix, where the biopolymer framework enhanced dye adsorption, nanoparticle dispersion, and overall photocatalytic efficiency [38]. Ferrite-supported polymer nanocomposites have also been reviewed as effective adsorbents and photocatalysts, highlighting the role of polymer matrices in increasing surface area and pollutant affinity while maintaining magnetic recovery capabilities [39]. Additionally, studies on spinel ferrite nanomaterials continue to emphasize the impact of synthesis and surface modification on visible-light activity and degradation efficiency, underscoring the importance of structural tuning in ferrite-based systems for organic pollutant removal [40]. These advances illustrate the growing interest in biopolymer-integrated ferrite photocatalysts that combine eco-friendliness, enhanced photocatalytic performance, and practical applicability while identifying ongoing challenges in stability, light-utilization, and real-water matrix effects [41,42]. The current research explores the guar-gum modified $ZrFe_2O_4$ BNC to improves interfacial interaction, visible-light photocatalyst, and reusability to have an efficient MG degradation. The reaction parameters including catalyst dose, irradiation time, pH, and initial dye concentration were optimized systematically by batch experiments to provide maximum degradation efficiency. In addition, kinetic behaviour, reactive species by scavenger studies and reusability add more information regarding MG degradation in the literature.

2. Methods and materials

2.1. Chemicals and reagents

Guar-gum, Ferric chloride ($FeCl_3.6H_2O$) and sodium hydroxide (NaOH) were sourced from the company Loba Chemie. Zirconyl nitrate ($ZrO(NO_3)_2.xH_2O$) was purchased from the company Qualikems Laboratory reagents. Malachite green dye, with a maximum absorbance λ_{max} = 617 nm, was purchased from Merck, India. Precise quantities of all salts and reagents were measured for use. The 1000 ppm stock solution of malachite green was prepared by dissolving an appropriate amount of dye in 100 mL of distilled water.

2.2. Green synthesis of GG@ZrFe BNC

The BNC was synthesized via an eco-friendly protocol that integrates the coprecipitation method and sol-gel method, employing biopolymer GG as a stabilizing and reducing agent. In 500 mL three-necked round bottom flask, a homogenous mixture was prepared by dissolving 2 g of GG 100 mL of deionized water. Separately, a solution of 1 g zirconyl nitrate ($ZrO(NO_3)_2.xH_2O$) and 0.5 g of ferric chloride ($FeCl_3.6H_2O$) was dissolved in 100 mL of distilled water. The two solutions were combined and placed on the magnetic stirrer. Subsequently, 25 mL of ammonia solution was added dropwise to the reaction mixture until brown precipitates formed, while maintaining the pH between 8 and 9. The mixture was continuously stirred for 4 h. The resulting precipitate was collected filtered, washed 4–5 times with distilled water, to remove the residual impurities, and finally dried in an oven at 60 °C for 5 h.

2.3. Characterisation of GG@ZrFe BNC

The GG@ZrFe BNC was characterized using a range of analytical techniques to elucidate its structural features, crystallinity, surface morphology, bonding interactions, and physicochemical properties. The functional groups and bond formation were analysed using Fourier transform infrared (FTIR) spectrophotometer (Perkin Elmer Spectrum PE1600, USA), operating in transmission mode over the range of 400–4000 cm^{-1}. The crystalline structure and lattice composition of ZrFe immobilized within the GG blend were investigated by X-ray Diffraction (XRD) using an Ultima diffractometer (Rigaku, Tokyo, Japan). The elemental composition and surface morphology were examined by scanning electron microscopy coupled with Energy diffraction X-ray analysis (SEM-EDX) using a JEOL GSM 6510LV, Japan. The size of particle and its distribution within biopolymer blend of GG were investigated using Transmission Electron Microscope (TEM, JEM 2100, Japan). To investigate the surface elemental composition and corresponding chemical states of the discrete elements via X-ray Photoelectron (XPS) spectroscopy (PHI 5000 Versa Probe II, FEI Inc.). To determine dynamic size of the synthesized material Zetasizer advance (Malvern Panalytical) was employed. The optical properties, band gap, and MG dye concentration during both before and after photocatalytic degradation, were evaluated by double beam UV–Vis spectrophotometer (Shimadzu UV-1900). The magnetic properties before and after functionalization of ZrFe NPs with the biopolymer matrix of GG were determined using vibrating sample magnetometry (VSM, PAR 155 Quantum Design, Lake Shore, USA).

2.4. Photocatalytic experiments

The photocatalytic degradation of MG using GG@ZrFe BNC was conducted under batch method with visible light source. A 25 mL MG solution was prepared at varying concentrations (10–50 mgL^{-1}), pH values (1–8), catalyst dose (5–25 mg), and irradiation time (5–30 min). The preliminary experiments were performed using a visible light source 300 W tungsten-halogen lamp (400–700 nm), placed 10 cm from the reactor, with a measured light intensity of 80 mW cm^{-2} at the solution surface. After each experiment, optimized values for each parameter were determined and used for kinetics studies and scavenger test. All photocatalytic degradation experiments were conducted in the triplicate ($n = 3$), and reported results as the mean values having standard deviations of ±2–3%, confirming the high reproducibility and reliability of the measurements. The photocatalyst efficiency was evaluate using UV–Vis spectrophotometer. The maximum absorption wavelength of MG was identified as $\lambda_{max} = 617$ nm and the percentage degradation of MG was calculated by using the following eq. (1).

$$\text{Photocatalytic efficiency}\ (\%) = \frac{C_0 - C_t}{C_0} \times 100 \quad (1)$$

here C_0 and C_t are the initial and final concentrations of MG, respectively, after the photocatalytic experiment. The experimental data was processed and analysed using MS excel and Origin 9.1 software to drive meaningful insights.

3. Results and discussion

3.1. Analytical techniques for characterisation

The FTIR spectra of GG, ZrFe NPs and GG@ZrFe BNC are presented in Fig. 1 (black, red, and blue line respectively). The observed bands correspond to the stretching and bending vibrations of specific functional groups. For GG, the spectrum displays distinct absorption peaks at 3278 cm^{-1} (–OH stretching), 2892 cm^{-1} (–CH vibrations), 1644 cm^{-1} (hydroxyl bending), 1413 cm^{-1} (C—H bending), 1014 cm^{-1} (C–OH bond) and 804 cm^{-1} (C–O–C bond) [43]. The FTIR spectra of ZrFe NPs examined 3245 cm^{-1} (–OH stretching), 1556 cm^{-1} (O—H bending of absorbed water molecules), 1346 cm^{-1} (Fe—Zr stretching), 844 cm^{-1} (C-OH), 695 (Fe—O) cm^{-1} and 580 cm^{-1} (Zr—O) [25]. The FTIR spectra of GG@ZrFe BNC (red line) examined absorption peaks at 3245 cm^{-1} (-OH stretching), 2892 cm^{-1} (-CH stretching), 1346 cm^{-1} (Fe—Zr stretching), 1027 cm^{-1} (O-Zr-O stretching), 804 cm^{-1} (C–OH bond), 701 cm^{-1} (Fe—O) and 688 cm^{-1} (Zr—O) [44].

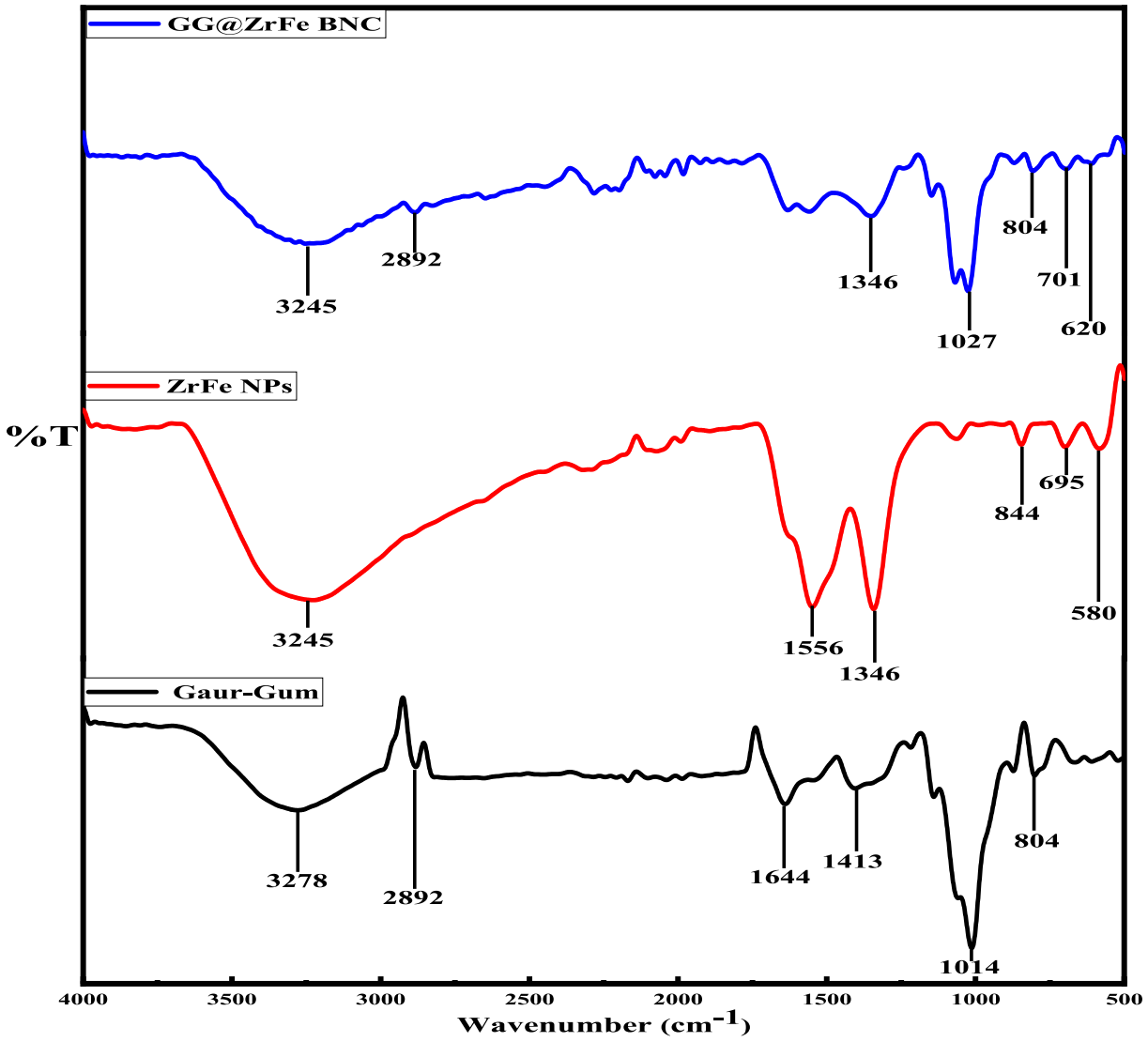

Fig. 1. FTIR spectra of GG, ZrFe NPs and GG@ZrFe BNC (black line, red line, and blue line respectively). (For interpretation of the references to colour in this figure legend, the reader is referred to the web version of this article.)

The powder XRD patterns of pristine ZrFe NPs and the GG-functionalized BNC (GG@ZrFe BNC) are shown in Fig. 2. Both samples exhibit distinct diffraction peaks that can be indexed to the orthorhombic zirconium ferrite phase, in good agreement with JCPDS card No. 22–1086. The most intense reflections appear at 2θ ≈ 11.8°, 23.9°, 32.2°, and 36.3°, which correspond to the (110), (211), (220), and (310) planes, respectively. The absence of any additional reflections from secondary oxides such as ZrO_2 or Fe_2O_3 confirms the phase purity of the synthesized materials. Compared with pristine ZrFe NPs, the GG@ZrFe BNC shows broader and less intense peaks. This broadening is indicative of a decrease in crystallite size and an increase in structural strain within the lattice, which arise from polymer capping and interfacial interactions between the inorganic phase and the GG matrix. Further quantitative analysis of XRD data for evaluation of crystallite size and lattice strain was done by eqs. (2–5) [45,46];

$$D = \frac{K\lambda}{\beta \mathrm{Cos}\theta} \tag{2}$$

$$d = \frac{\lambda}{2\mathrm{Sin}\theta} \tag{3}$$

$$\varepsilon = \frac{\beta \mathrm{Cos}\theta}{4\mathrm{Sin}\theta} \tag{4}$$

$$\delta = \frac{1}{D^2} \tag{5}$$

Where, D (crystallite size), d (interlayer spacing), ε (Micro-strain), δ (dislocation density), λ (1.54 Å CuKα radiation), K (0.9 spacing factor). Scherrer analysis of the principal peaks revealed that the average crystallite size decreases from 25 to 30 nm for ZrFe NPs to 15–18 nm for GG@ZrFe BNC, highlighting the growth-restricting role of the biopolymer. The corresponding dislocation density (δ) increased from 1.3×10^{-3} nm^{-2} in ZrFe to 3.7×10^{-3} nm^{-2} in the composite, consistent with a higher defect density. Williamson–Hall analysis provided further insights into the microstructural evolution. The microstrain (ε) was estimated to be 2.1×10^{-3} for pristine ZrFe, while the value nearly doubled to 4.8×10^{-3} in the GG@ZrFe composite. This increased strain is attributed to the incorporation of flexible GG chains, which impose stress on the Zr-Fe-O lattice and enhance defect sites. Such defects, coupled with reduced crystallite size, are beneficial for photocatalytic applications. Thus, XRD confirms that while the crystalline ZrFe structure is preserved after functionalization, the polymer anchoring significantly modifies the crystallite size and strain, producing a defect-rich nanocomposite with enhanced physicochemical properties.

Fig. 3 (a-d) shows the SEM images used to analysed the surface morphology of the GG@ZrFe BNC. ZrFe NPs shown in Fig. 3 (a) exhibit a porous structure with irregular shaped particles. Fig. 3 (b, c) reveals SEM image of GG@ZrFe BNC captured at 1000 and 10,000 magnification range. Fig. 3 (b) shows the formation of GG biopolymer which appears spherical, powdered, agglomerated clusters distributed over the surface confirming the GG@ZrFe BNC. Fig. 3 (d) illustrates the energy dispersive X-ray (EDX) spectrum of the synthesized material, depicting its elemental composition over an energy range from 1 to 20 keV. The corresponding elemental weight percentage (%) composition includes C K (24.7%), O K (28.2%), Fe (31%) and Zr L (16.1%), while the atomic percentage (%) are C K (45.2%), O K (38.7%), Fe (12.2%) and Zr L (3.9%). These findings confirm the purity of the synthesized material. As shown in Fig. S1 (a-e), selected area SEM image and elemental distribution of maps C, O, Zr and Fe, demonstrates the high purity of the synthesized material and the absence of any impurities.

The morphology characteristics and particle size distribution of the synthesized nanomaterials were evaluated through TEM analysis. According to Fig. 4 (a), the TEM image indicates that the particles are almost spherical in shape and having a homogenous distribution with a slight agglomeration. The NPs are also found to be well-dispersed in the form of porous and loosely connected network, which can be useful in the applications like photocatalysis due to enhanced surface area and active sites are exposed. In order to measure particle size distribution, statistical analysis was carried out on multiple particles extracted from the TEM image, and the results are presented in Fig. 4 (b). The histogram, fitted with a Gaussian curve, indicates that the particle sizes follow a normal distribution. The calculated mean particle size (μ) is approximately 11.20 nm, with a standard deviation (σ) of 2.72 nm. This narrow distribution suggests that the synthesis process produced

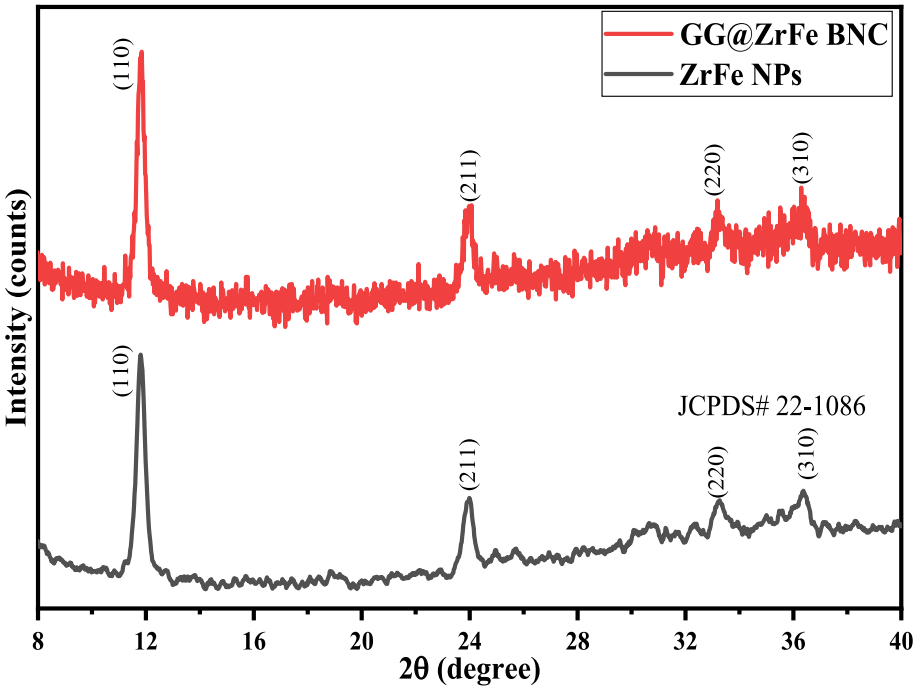

Fig. 2. XRD spectra of ZrFe NPs and GG@ZrFe BNC (black line and red line respectively). (For interpretation of the references to colour in this figure legend, the reader is referred to the web version of this article.)

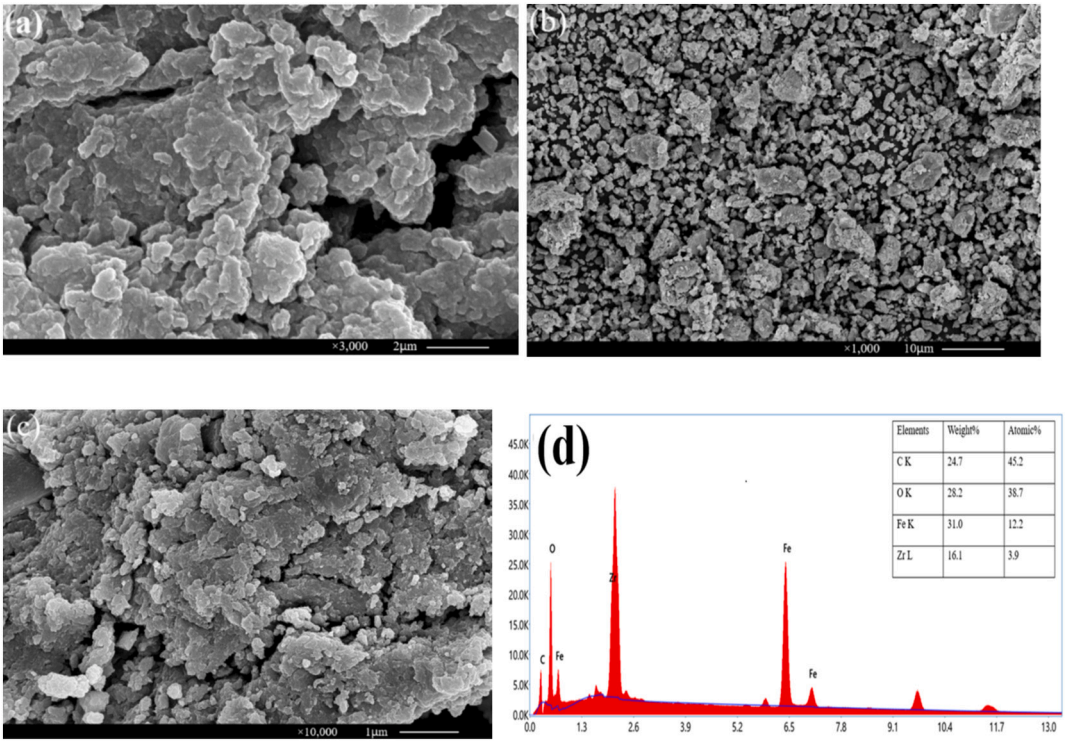

Fig. 3. SEM image of (a) ZrFe NPs, (b) GG@ZrFe BNC at 1000 magnification, (c) GG@ZrFe BNC at 10000 magnification and (d) EDX spectra with mapping of GG@ZrFe BNC.

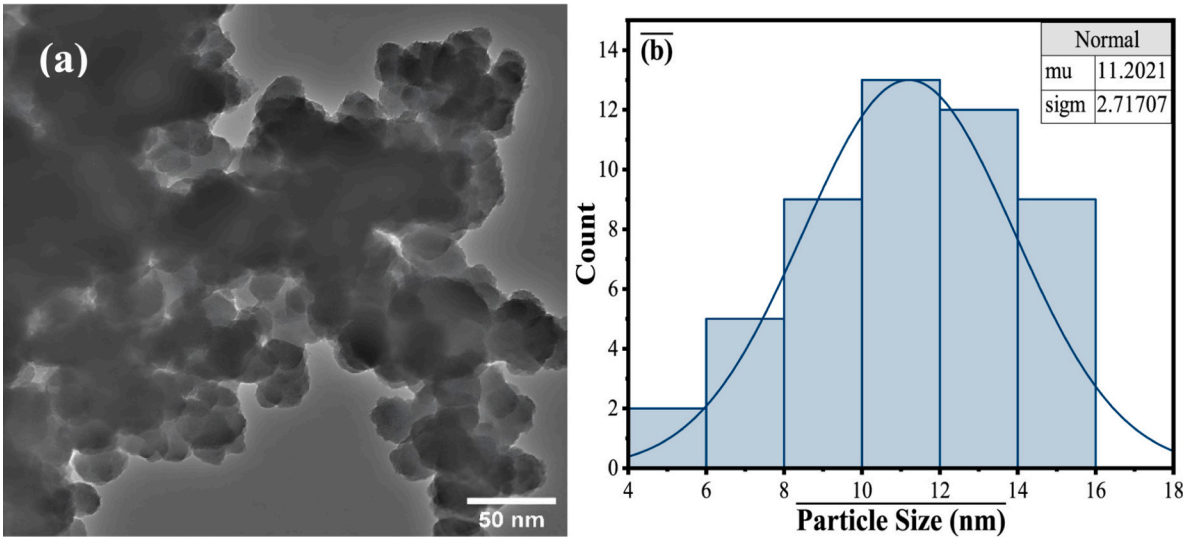

Fig. 4. (a) TEM image and (b) Gaussian distribution profile for particle size of GG@ZrFe BNC.

relatively uniform nanoparticles, which is critical for ensuring the consistent physical and chemical properties.

The optical absorption and the energy band gap of the synthesized GG@ZrFe BNC were evaluated using UV–Vis spectroscopy within the wavelength range of 200–650 nm, as illustrated in Fig. 5 (a). The spectrum reveals two absorption maxima of GG@ZrFe BNC at 270 nm corresponding to n-π* transitions and at 379 nm, indicating a red shift due to surface functionalization, immobilization, and stabilization of ZrFe NPs by the GG biopolymer blend. As shown in the inset of Fig. 5 (a) the band gap energy (E_g) of the semiconductor was determined from the Tauc plot according to eq. (2) [47]:

$$\alpha h\nu = A\left(h\nu - E_g\right)^n \quad (2)$$

In his relation, α corresponds to the absorption coefficient, v is frequency of radiations, h denotes Planck's constant, A is constant, and n characterizes the type of electronic transition with $n = 2$ for direct transitions and $n = 1/2$ for indirect transitions. The calculated band gap energy for the synthesized material GG@ZrFe BNC was 1.23 eV, indicating that immobilization reduced the band gap, thereby enhancing photocatalytic activity. For comparison, literature reports a band gap of 2.05 eV for bulk ZrFe NPs. The observed band gap reduction is attributed to the quantum confinement contraction resulting from the functionalization of ZrFe with the GG biopolymer blend [25].

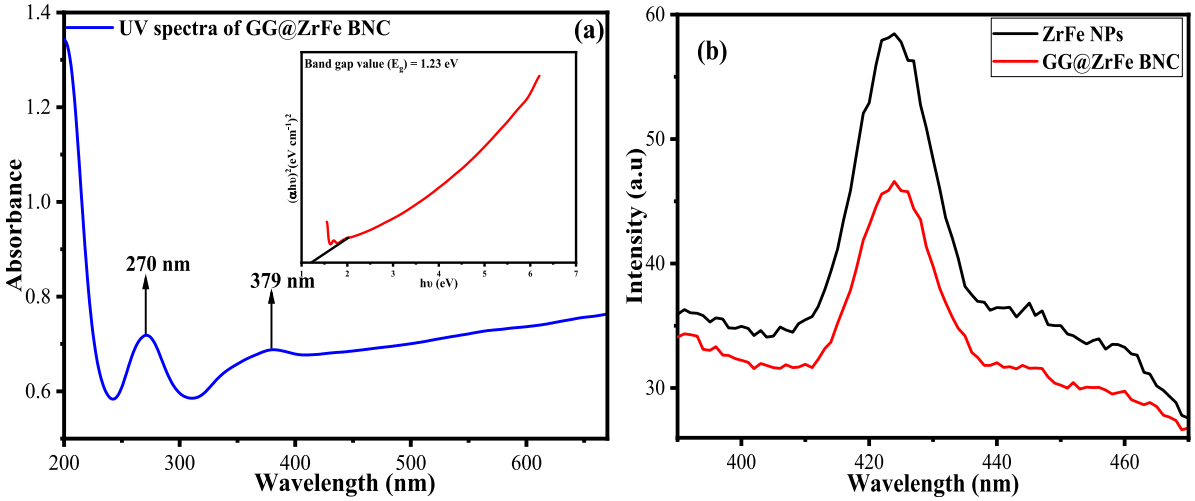

Fig. 5. UV–Vis spectra of GG@ZrFe BNC and inset corresponding Tauc's plot for the evaluation of band gap energy (b) Photoluminescence spectra of ZrFe NPs and GG@ZrFe BNC.

The photoluminescence (PL) spectra of ZrFe and GG@ZrFe BNC were analysed, and results are presented in Fig. 5 (b). PL spectroscopy provides insights into defects states and electron-hole recombination pathways in the material. ZrFe NPs shows strong PL emission, associated with rapid recombination of photogenerated carriers. In GG@ZrFe BNC, the suppressed PL response suggests reduce recombination, likely due to the GG-induced interfacial charge carrier trapping and enhanced separation of electron and holes. The interaction between GG molecules and the electronic structure of ZrFe effectively facilitates charge separation, thereby suppressing electron-hole recombination and enhancing the material's photocatalytic efficiency.

XPS studies was utilized to determine the surface elemental composition and corresponding chemical states of GG@ZrFe BNC. Fig. 6 (a) shows the survey scan of GG@ZrFe BNC which explained that C, O, Zr and Fe are the main elements of the material. Fig. 6 (b) represents the C1s spectrum have binding energies with triplet peaks at 284.9 eV, 286.7 eV and 288.8 eV which are related with C–C/C–H, C═O and O-C=O respectively are in the material attached to GG chain [48]. Fig. 6 (c) represents the O1s spectrum having binding energies with triplet peaks at 534.2 eV, 532.7 eV and 531.2 eV which are related with Zr—O, O^{2-} and O—H respectively [49]. Fig. 6(d) displays the high-resolution Zr 3d XPS spectrum with characteristic peaks at 181.9 eV (Zr $3d_{5/2}$) and 184.2 eV (Zr $3d_{3/2}$), corresponding to the spin-orbit components of Zr^{4+} in the zirconyl ferrite matrix. Deconvolution of the spectrum yields a single Zr $3d_{5/2}$-Zr $3d_{3/2}$ doublet with a spin-orbit splitting of 2.3 eV, confirming the absence of mixed oxidation states and indicating strong lattice incorporation of Zr^{4+} rather than surface contamination. Fig. 6(e) presents the high-resolution Fe 2p XPS spectrum showing two prominent peaks centered at 710.8 eV (Fe $2p_{3/2}$) and 724.5 eV (Fe $2p_{1/2}$), along with a characteristic satellite feature around at 720.7 eV, which is a diagnostic signature of Fe^{3+} species. Deconvolution of the Fe $2p_{3/2}$ region reveals components associated with Fe—O bonding, while the absence of peaks corresponding to Fe^{2+} or metallic Fe confirms that iron exists predominantly in the trivalent oxidation state within the zirconyl ferrite lattice [50]. Compared with reference binding energies of pure ZrO_2 and Fe_2O_3, the positive shift observed here is attributed to strong Fe-O-Zr interfacial bonding and charge redistribution within the mixed-oxide lattice, rather than surface contamination or mixed oxidation states [51,52].

The magnetic properties of ZrFe NPs before and after GG functionalization were examined using VSM. The observed narrow hysteresis loop indicates soft magnetic behaviour, while the M-H profile shown in Fig. 7 confirms the super magnetic material. The saturation magnetization is achieved at approximately 6000 Oe with magnetic moment (m_s) of 4.7 $emug^{-1}$, which is advantageous for the magnetic separation.

Zeta potential measurements were carried out to determine the point of point of zero charge and to examine the pH-dependent adsorption behaviour of MG on GG@ZrFe BNC. A 25 mL solution of 0.1 M KCl was prepared as a background electrolyte with 20 mg of the catalyst and sonicated for 15 min to ensure uniform distribution. The solution pH was adjusted to a range of pH 1 to pH 10 and measurements were taken at one-unit intervals after 12 h of dispersion time. The results, presented Fig. S2, shows a decrease in zeta potential from 37.0 mV at pH 1 to 6.5 mV at pH 10, with the zeta potential approaching approximately 0 mV at pH 3.9. This pH represents the isoelectric point (IEP) or point of zero charge (PZC) catalyst surface, and the corresponding pH values is referred to as pH_{iep} or pH_{pzc}.

3.2. Photocatalytic activity

3.2.1. Role of leaching test

The series of experiments were conducted to evaluate the dye removal performance under the following three conditions: (1) catalyst with visible light (photocatalysis), (2) catalyst without visible light (adsorption), and (3) visible light without a catalyst (photolysis). The experiments were conducted at pH 7, with 10 mg L^{-1} MG concentration, 20 mg of catalyst dose, and 30 min of irradiation time. Fig. 8 (a) illustrates a continuous increase in the %degradation of MG dye with increasing irradiation time when both the catalyst and a tungsten-halogen lamp are applied, resulting in approximately 91% dye removal after 30 min. In contrast, photolysis resulted in only 7% degradation, while adsorption achieved 64% degradation. These findings indicate that the highest efficiency in dye degradation was achieved through photocatalysis, demonstrating its superiority as a method for dye removal compared to photolysis or adsorption.

3.2.2. Role of initial dye concentration

The role of different initial MG concentration on the photocatalytic performance and %degradation of catalyst was investigated using 20 mL of aliquot of MG solutions (10–50 ppm) with 20 mg of catalyst in the presence of visible light. Fig. S3 (a, b) illustrates the relationship between MG concentration and %degradation. Fig. S3 (b) represents the standard deviation used to determine the error bars, and confirms the reproducibility and reliability of experimental results of photocatalytic degradation at various MG concentrations in Table S2. It was found out that as the MG concentration increased from 10 to 50 ppm, an abnormal behaviour in %degradation was observed. The %degradation values for different MG concentrations were calculated from the UV–Vis spectra as

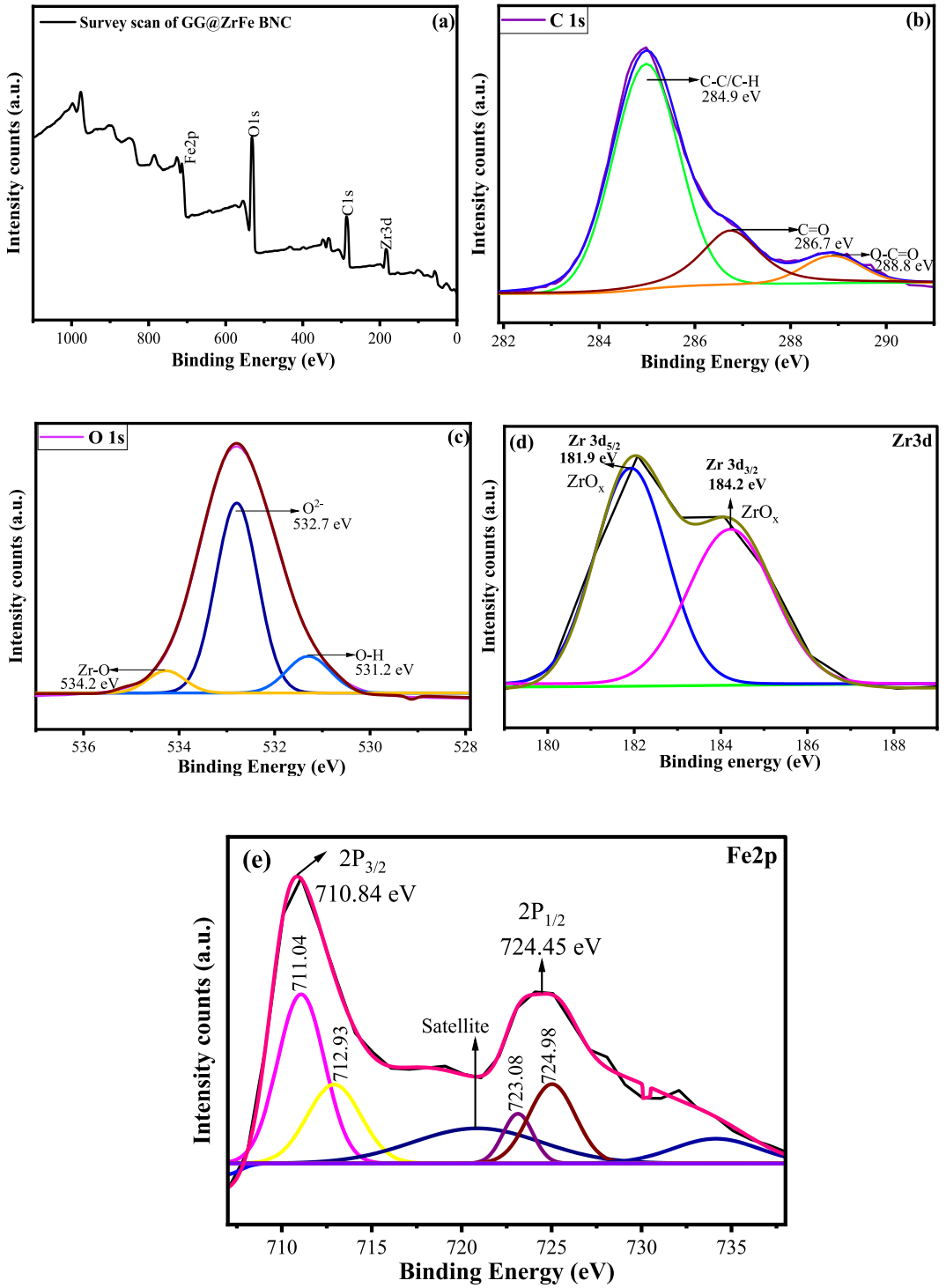

Fig. 6. X-ray photoelectron spectra of GG@ZrFe BNC (a) survey spectrum, (b) C1s, (c) O1s, (d) Zr3d and (e) Fe2p.

follows- 97.48%; 10 mg L^{-1}, 94.02%; 20 mg L^{-1}, 98.33%; 30 mg L^{-1}, 99.79%; 40 mg L^{-1} and 91.26%; 50 mg L^{-1}. The highest degradation efficiency (99.79%) was achieved 40 mg L^{-1}, making it the optimal concentration maximum photodegradation minimal screening effects. At higher MG concentrations, the dye molecules absorb significant portion of incident light, leading to a screening effect that limits the activation of photocatalyst and the limited number of active adsorption sites on the catalyst surface becomes saturated, further hindering the degradation process.

3.2.3. *Role of pH*

The role of pH on the degradation of MG was studied at concentration of 40 mgL^{-1} under identical experimental conditions. Since photocatalysis involves the accumulation of dye molecules on the surface of the catalyst, the solution pH plays a crucial role in influencing the binding process. Fig. S4 (a, b) illustrates the relationship between pH and %degradation of MG. The error bar in Fig. S4 (b) indicates that the results of the photocatalytic degradation are good to be reproducible in the entire pH range that was examined in Table S3. The degradation efficiencies obtained were as follows: 49.74%; pH 1, 77.99%; pH 2,

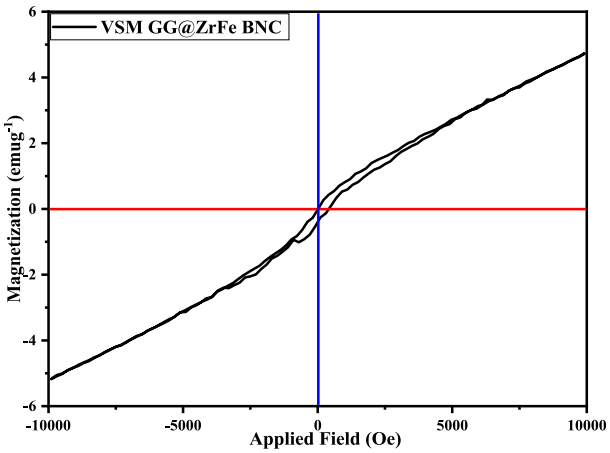

Fig. 7. Magnetization versus applied magnetic field curve for GG@ZrFe BNC at 25 °C.

87.76%; pH 3, 93.15%; pH 4, 95.86%; pH 5, 97.38%; pH 6, 98.37%; pH 7 and 99.33%; pH 8. The indicate that the catalyst surface charge varies with pH due to protonation and deprotonation of the surface functional groups. As the pH increases, the degradation also increases, because of the increased generation of hydroxyl radical ($OH^{\bullet}$) at higher pH levels and the higher negative charge density on the catalyst surface. This negative charge enhances the electrostatic attractions of the positively charged MG molecules, resulting in more efficient degradation. Therefore, the highest degradation efficiency (99.33%) was achieved at pH 8, making it the optimal pH for the maximum photodegradation.

3.2.4. Role of catalyst dose loaded

The role of catalyst dose on MG degradation was studied at concentration of 40 mgL^{-1}, pH 8 and irradiation time of 30 mins under identical experimental conditions. Fig. S5 (a, b) illustrates the relationship between catalyst dose and %degradation of MG. The degradation efficiencies obtained were as follows: 72.23%; 5 mg, 82.81%; 10 mg, 91.53%; 15 mg, 99.57%; 20 mg, and 89.31%; 25 mg. The error bar in Fig. S5 (b) indicates that the results of the photocatalytic degradation are good to be reproducible in the entire catalyst dose range that was examined in Table S4. The result reveal that increasing the catalyst dose from 5 mg to 20 mg provides more active on the catalyst surface for the dye molecules to adsorb which will enhances the interaction between the dye molecules and catalyst, leading to improved photocatalytic degradation efficiency. However, at higher doses, such as 25 mg, the catalyst surface becomes saturated with dye molecules. Once saturation occurs, additional catalyst does not significantly increase degradation efficiency because no further adsorption sites are available. Therefore, the optimal MG degradation efficiency was achieved at a catalyst dose of 20 mg.

3.3. Role of irradiation time and Kinetics of Reaction

The role of irradiation time on the degradation of MG was studied at concentration of 40 mgL^{-1} and pH 8 under identical experimental conditions. Fig. S6 (a, b) illustrates the relationship between irradiation tine and %degradation of MG. The error bar in Fig. S6 (b) indicates that the results of the photocatalytic degradation are good to be reproducible in the entire irradiation time range that was examined in Table S5. The degradation efficiencies obtained were as follows: 75.12%; 5 mins, 83.76%; 10 mins, 89.91%; 15 mins, 93.55%; 20 mins, 96.69%; 25 mins and 99.88%; 30 mins. As the irradiation time increases, the extent of

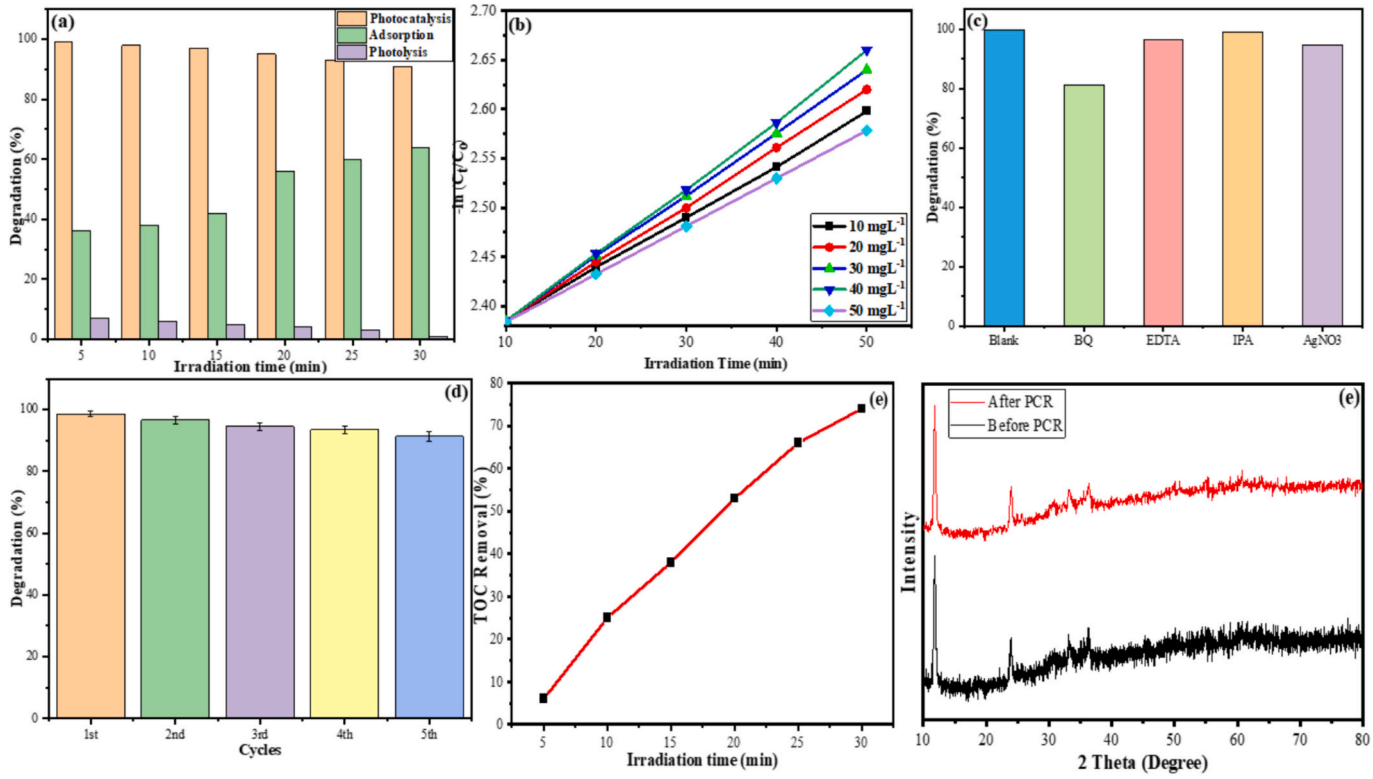

Fig. 8. (a) Bar graph of irradiation time vs % degradation demonstrating the leaching test, (b) (c) –ln (C_t/C_0) vs irradiation time for 10–50 mg L^{-1} MG concentration for the photocatalytic degradation of MG by GG@ZrFe BNC, (c) Bar graph of % degradation vs different types of scavenger for the identification of ROS, (d) Reusability experiment for GG@ZrFe BNC; error bar represents the standard error and (e) total organic carbon (MG concentration = 40 mg L^{-1}, catalyst dose = 20 mg, pH = 8 and irradiation time = 30 min), and (f) XRD spectra of GG@ZrFe BNC before (black line) and after (red line) photocatalytic reactor. (For interpretation of the references to colour in this figure legend, the reader is referred to the web version of this article.)

photocatalytic degradation improves due to prolonged exposure of the dye molecules to the active sites of the catalysts and photon absorption. Each absorbed photon generates electron-hole pairs that actively participate in breaking down the dye molecules. This prolonged exposure enhances this process, enabling a higher number of dye molecules to be degraded, thereby improving overall efficiency. Therefore, the maximum MG degradation efficiency was achieved at 30 mins of irradiation time.

The photocatalytic degradation of MG dye using GG@ZrFe BNC was studied by varying the irradiation time under visible light to evaluate the reaction kinetics. The experiments were conducted with a catalyst dose of 20 mg, irradiation time ranging from to 10–60 min, and MG concentrations between 10 and 50 mg L^{-1} at pH 8. The results confirmed that the degradation process follows pseudo-first-order kinetics. The pseudo-first-order kinetics were analysed using the following equation related to half-life period [53]:

$$-\ln\frac{C_t}{C_o} = kt \tag{5}$$

$$t_{1/2} = \frac{0.693}{k} \tag{6}$$

where C_0 and C_t represent the initial and final concentrations of MG after time t, k_1 is the rate constant for pseudo-first-order reaction and $t_{1/2}$ is the half-life.

The kinetic graph, presented on Fig. 8 (b), shows a linear relationship between –ln (C_t/C_0) and the irradiation time, with the slope corresponding to the rate constant k_1. The apparent first-order rate constant (k_1) increased steadily from 0.01 min^{-1} to 0.03 min^{-1} as the MG concentration rose from 10 to 30 mg L^{-1}, suggesting improved interaction between dye molecules and the active photocatalyst sites. From Table 1, it can be seen that a maximum rate constant of 0.09 min^{-1} was observed at 40 mg L^{-1}, indicating an optimal concentration at which light absorption, active site availability, and generation of reactive oxygen species were most effectively balanced. However, at 50 mg L^{-1}, the rate constant decreased slightly to 0.07 min^{-1}, likely due to excessive dye molecules causing light shielding and surface site saturation, which hinder the photocatalytic activity. These results demonstrate that GG@ZrFe exhibits promising photocatalytic efficiency, with optimal degradation performance at moderate MG concentrations.

3.4. Trapping experiment and determination of ROS

Radical scavenging experiments were performed with four specific quenchers to determine the reactive species in the process of photocatalytic degradation of MG: isopropyl alcohol (IPA) to trap hydroxyl radicals ($^{\bullet}OH$) [54], benzoquinone (BQ) to trap superoxide radicals ($O_2^{\bullet-}$) [55], EDTA to trap photogenerated holes (h^+) [56], and $AgNO_3$ to trap conduction-band electrons (e^-) [57]. The experiments were conducted with optimum conditions (40 mg L^{-1} MG, 20 mg catalyst, pH 8, 30 min visible light irradiation), the resulting changes in degradation efficiency were recorded to evaluate the contribution of each reactive species. The presence of BQ significantly reduced the degradation efficiency, confirming that superoxide radicals ($O_2^{\bullet-}$) play dominant reactive species that promotes the process of photocatalytic oxidation of MG.

Table 1
The pseudo first order kinetic parameters for photodegradation of MG using GG@ZrFe BNC.

S. N.	MG concentration (mg L^{-1})	Rate constant (k_1) (min^{-1})	Half-life $t_{1/2}$ (min)	R^2
1	10	0.01	69.3	0.99
2	20	0.02	34.6	0.99
3	30	0.03	23.2	0.99
4	40	0.09	7.7	0.99
5	50	0.07	9.9	0.99

Conversely, when IPA was added, the degradation was reduced a minor, demonstrating that $^{\bullet}OH$ radicals play a secondary role in the reaction pathway. The addition of EDTA resulted in an intermediate decrease in activity, which suggests that photogenerated holes (h^+) are involved in secondary oxidation reactions, but are not the primary oxidizing agents. Lately, when $AgNO_3$, an efficient scavenger of electron was added, the performance of degradation was significantly reduced, which suggests that conduction-band electrons play an important role in the formation of $O_2^{-}\bullet$ in the presence of oxygen reduction. Overall, the order of influence of scavengers on photocatalytic efficiency as shown in Fig. 8 (c) followed: BQ> > $AgNO_3$ > EDTA>IPA, which confirms that $O_2^{\bullet-}$ radicals dominate the reaction mechanism, supported by electron transfer from the GG@ZrFe conduction band to dissolved oxygen. These results are consistent with the band structure of the material and align with the proposed mechanism involving superoxide-driven degradation with minor contributions from h^+ and $^{\bullet}OH$.

The mechanism of MG degradation by GG@ZrFe BNC can be described as follows [58,59]:

$$GG@ZrFe + hv \rightarrow GG@ZrFe\left(h^-_{VB} + e^-_{VB}\right) \tag{i}$$

$$GG@ZrFe\left(h^-_{VB}\right) + H_2O \rightarrow GG@ZrFe + H^+ + {}^{\bullet}OH \tag{ii}$$

$$GG@ZrFe\left(e^-_{VB}\right) + O_2 \rightarrow GG@ZrFe + O_2^{-\bullet} \tag{iii}$$

$$O_2^{-\bullet} + H^+ \rightarrow HO_2^{\bullet} \tag{iv}$$

$$GG@ZrFe\left(e^-_{CB}\right) + HO_2^{\bullet} + H^+ \rightarrow H_2O_2 \tag{v}$$

$$GG@ZrFe\left(e^-_{CB}\right) + H_2O_2 \rightarrow OH^{\bullet} + OH^- \tag{vi}$$

$$MG + O_2^{-\bullet} \rightarrow MG - OO \rightarrow \text{Degraded products} \tag{vii}$$

Upon visible light irradiation, the GG@ZrFe bionanocomposite generates electron-hole pairs, initiating a series of radical-driven reactions responsible for the degradation of MG. The photogenerated electrons in the conduction band rapidly reduce dissolved oxygen molecules to form superoxide radicals ($O_2^{\bullet-}$), which are identified as the dominant reactive species through trapping experiments. These $O_2^{\bullet-}$ radicals first attack the central carbon atom of the MG chromophore, promoting successive *N*-demethylation steps and weakening the π-conjugated structure. Continued oxidative stress leads to chromophore fragmentation, ultimately causing ring-opening reactions that dismantle the aromatic framework. Meanwhile, photogenerated holes (h^+) participate in secondary oxidation reactions, producing small amounts of $^{\bullet}OH$ from water, which further assist in breaking down intermediate fragments. The sequential transformation yields low-molecular-weight products, including aldehydes, alcohols, and short-chain carboxylic acids, which align with TOC reduction trends. This combined action of $O_2^{\bullet-}$, h^+, and minor $^{\bullet}OH$ contributions complete the progressive mineralization pathway, converting MG into simpler, less toxic organic compounds.

3.5. Reusability experiment and TOC analysis of GG@ZrFe BNC

Reusability experiments were conducted to evaluate the stability of the synthesized GG@ZrFe BNC and assess its economic and environmental sustainability for water treatment applications. After each photocatalytic experiment, the catalyst was recovered via centrifugation, washed repeatedly with distilled water, and dried before being reused. The experiments were performed under optimized conditions: 40 mg L^{-1} MG concentration, 20 mg catalyst dose, pH 8, and 30 min under exposure of visible light. Fig. 8 (d) demonstrates that the catalyst maintained high photocatalytic efficiency over five consecutive cycles, with degradation value of 98.65% after the first cycle, 96.61% after second, 94.5% after third, 93.45% after fourth, and 91.34% after fifth

cycle. The error bar in Fig. 8 (d) show the standard error in which the estimates were based on several independent experimental run per cycles. The SE values indicates that the experiments have good reproducibility and the GG@ZrFe BNC has constant photocatalytic activity in repeat reuse cycles in Table S6. These finding confirm that GG@ZrFe BNC display high photocatalytic activity exceeding five cycles, having strong potential to recycle MG dye under visible light. ICP-OES was also used to determine the chemical stability of the GG@ZrFe photocatalyst in terms of the release of Zr and Fe ions under photocatalysis conditions. After 30 min of visible light irradiation, both ions were not below 0.5 mg L^{-1} shows the negligible leaching. This proves that the guar-gum matrix is effective in stabilizing $ZrFe_2O_4$ NPs and avoiding dissolution upon operation, confirming the environmental safety and high performance in the long-term.

Fig. 8 (e) illustrates the TOC removal efficiency of MG as a function of irradiation time in photocatalysis process in the presence of the GG@ZrFe BNC. TOC analysis gives a direct indication of the degree of mineralization, which indicates the transformatio of organic carbon into CO_2 and H_2O. TOC removal is increasing steadily with irradiation time with a rise of about 12% at 5 min up to about 74% at 30 min. This steadily increasing trend indicates that the produced reactive species do not only decolorize MG, but also gradually break down its aromatic structure into smaller, less complex molecules. The high degree of mineralization within only 30 min indicates the high efficiency and strong oxidative capability of the GG@ZrFe BNC. Although the complete mineralization (100%) was not obtained during the tested time frame, the high level of TOC decrease is the evidence of significant degradation of the dye as opposed to the cleavage of the chromophore.

Fig. 8 (f) reveals the XRD patterns of the GG@ZrFe photocatalyst before and after the photocatalytic reaction (PCR) to give insight into the structural stability of the material during repeated irradiation and degradation cycles. The pattern of diffraction captured before PCR (black curve) has typical peaks of orthorhombic $ZrFe_2O_4$, validates the crystalline structure of the BNC. After photocatalysis, the XRD pattern (red curve) has the same set of reflections without the addition of any new peaks indicating ZrO_2, Fe_2O_3, or other secondary phases. This means that there was no change in phase transformation, no crystallite decomposition, or no photocorrosion process in the degradation process. A slight reduction in peak intensity and minor broadening is observed in the post-reaction pattern, which may be attributed to surface restructuring, slight loss of long-range order, or increased defect density induced by repeated irradiation. However, the preservation of all major diffraction peaks confirms that the crystal framework of $ZrFe_2O_4$ remains intact, demonstrating the excellent structural robustness of the GG@ZrFe photocatalyst.

3.6. Role of various water matrix

Fig. S7 shows the role of common inorganic salts and natural organic matter in the photocatalytic degradation of MG over GG@ZrFe. The highest degradation efficiency (99.79%) is observed in deionized water, confirming the intrinsic activity of the catalyst. The presence of Na_2SO_4 (10 mM) slightly reduces the efficiency (95.28%) due to increased ionic strength and partial surface charge screening, while a more pronounced decrease in $CaCl_2$ (5 mM) (92.63%) is attributed to divalent Ca^{2+} ions causing stronger electrostatic neutralization and partial aggregation of catalyst particles. In the case of $NaHCO_3$ (10 mM), the efficiency remains relatively high (94.02%), indicating limited radical scavenging under the studied conditions. The addition of humic acid (5 mg L^{-1}) and fulvic acid (5 mg L^{-1}) leads to further reductions (93.18% and 90.43%, respectively), which can be ascribed to light-shielding effects, competitive adsorption on active sites, and scavenging of reactive oxygen species by organic matter, with fulvic acid showing a stronger inhibitory effect due to its lower molecular weight and higher mobility. From these results it can be observed that the GG@ZrFe photocatalyst maintained high degradation efficiency across all tested matrices, demonstrating strong resistance to matrix interference and good suitability for practical wastewater treatment applications [60,61].

3.7. Comparison with the literature

The photocatalytic degradation of MG was evaluated using the synthesized catalyst GG@ZrFe BNC under various parameters, including pH, dye concentration, catalyst dose, irradiation time and percentage degradation. As presented in Table 2, the results demonstrated that the GG@ZrFe BNC catalyst exhibited superior efficiency in degrading MG dye compared to other tested material.

4. Conclusion

In this study, a sustainable GG@ZrFe bionanocomposite was successfully synthesized by immobilizing zirconyl ferrite nanoparticles within a guar-gum matrix. Comprehensive characterisation confirmed the successful formation and stabilization of the composite: FTIR verified the functional groups of guar-gum and metal-oxygen vibrations of $ZrFe_2O_4$; XRD revealed the orthorhombic crystalline phase of $ZrFe_2O_4$ with no impurity peaks; SEM–EDX and TEM analyses showed uniform dispersion of ferrite nanoparticles within the biopolymer network with sizes in the nanometre range; XPS confirmed the presence of Zr^{4+}, Fe^{3+}, oxygen vacancies, and strong GG-ZrFe interfacial interactions; zeta potential measurements showed positive surface charge favourable for cationic dye interaction; UV–Vis/PL analyses indicated a narrowed band gap and efficient charge separation; and VSM confirmed soft magnetic behaviour suitable for assisted recovery. The GG@ZrFe composite demonstrated excellent photocatalytic efficiency, achieving 99.79% MG degradation in 30 min under optimized visible irradiation. The reaction followed pseudo-first-order kinetics ($R^2 = 0.99$), with rate enhancement at higher dye concentrations. Trapping experiments identified superoxide radicals ($O_2^{\bullet}$) as the dominant reactive species governing the degradation mechanism, supported by limited $^{\bullet}OH$ and h^+ contributions. TOC analysis confirmed substantial mineralization of MG. Structural stability was validated through post-reaction XRD and negligible ion leaching, confirming excellent durability and reusability over repeated cycles. The green synthesis route, low cost of materials, high activity, and strong stability underscore the practical potential of GG@ZrFe for scalable wastewater treatment. Scalability is inferred from the low-cost, benign synthesis and material composition; however, large-scale or continuous-flow tests were not conducted, and challenges such as biopolymer stability and fouling will be addressed in future work.

CRediT authorship contribution statement

Akshara Bassi: Writing – review & editing, Writing – original draft, Software, Methodology, Investigation. **Parvathalu Kalakonda:** Writing – review & editing, Writing – original draft, Visualization, Validation. **Mohammad Aslam:** Writing – review & editing, Writing – original draft, Visualization, Software, Conceptualization. **Imran Hasan:** Writing – review & editing, Writing – original draft, Visualization, Validation, Supervision, Software, Resources, Project administration, Methodology, Investigation, Funding acquisition, Formal analysis, Data curation, Conceptualization.

Consent for publication

Not applicable.

Ethics approval and consent to participate

Not applicable.

Table 2
Comparison of photocatalytic activity in the present study with reported literature.

Material	Light Source	MG concentration (mg L^{-1})	Irradiation time (min)	Catalyst dose (mg)	Degradation (%)	Reference
$LaFeO_3$	Sunlight	10	80	30	82	[62]
$CoFe_2O_4$/mpg-C_3N_4	UV	10	120	8	93.41	[63]
Ag-BFO	CFL	10	240	1	89.8	[64]
$CuFe_2O_4$	Sunlight	60	140	50	87.5	[65]
rGO-Fe_3O_4/TiO_2	Vis	5.5	55	15	99	[66]
ZnO/CNT	Visible light	30	60	10	79	[67]
GO-ZnO/Mn_2O_3	Sunlight	100	30	20	98.75	[68]
GG@ZrFe	Visible	40	30	20	99.79	Present study

Funding

This research received no external funding.

Declaration of competing interest

The authors declare that they have no known competing financial interests or personal relationships that could have appeared to influence the work reported in this paper.

Acknowledgments

The authors extend their thanks to Ongoing Research Funding Program (ORF-2025-670), King Saud University, Riyadh, Saudi Arabia.

Appendix A. Supplementary data

Supplementary data to this article can be found online at https://doi.org/10.1016/j.jwpe.2026.109745.

Data availability

Data will be made available on request.

References

[1] M. Adel, M.A. Ahmed, A.A. Mohamed, Synthesis and characterization of magnetically separable and recyclable crumbled MgFe2O4/reduced graphene oxide nanoparticles for removal of methylene blue dye from aqueous solutions, J. Phys. Chem. Solids 149 (2021) 109760.
[2] H. Kiwaan, T. Atwee, E. Azab, A. El-Bindary, Photocatalytic degradation of organic dyes in the presence of nanostructured titanium dioxide, J. Mol. Struct. 1200 (2020) 127115.
[3] A. Dehbi, Y. Dehmani, H. Omari, A. Lammini, K. Elazhari, S. Abouarnadasse, A. Abdallaoui, Comparative study of malachite green and phenol adsorption on synthetic hematite iron oxide nanoparticles (α-Fe2O3), Surf. Interfaces 21 (2020) 100637.
[4] H. Khawaja, E. Zahir, M.A. Asghar, M.A. Asghar, Graphene oxide decorated with cellulose and copper nanoparticle as an efficient adsorbent for the removal of malachite green, Int. J. Biol. Macromol. 167 (2021) 23–34.
[5] S. Salamat, M. Hadavifar, H. Rezaei, Preparation of nanochitosan-STP from shrimp shell and its application in removing of malachite green from aqueous solutions, J. Environ. Chem. Eng. 7 (5) (2019) 103328.
[6] Himanshi, B. Lal, A. Verma, Suman, J. Ahmed, A. Singh, C. Choon Kit, R. Jasrotia, N. Lakshmaiya, V. Mehra, Insights into the photocatalytic removal of malachite green organic pollutant by highly efficient hard responsive Ba1− xCoxDyyFe12−yO19 catalysts, Sci. Rep. 15 (1) (2025) 1225.
[7] S.B. Zadvarzi, M. Khavarpour, S.M. Vahdat, S.M. Baghbanian, A.S. Rad, Synthesis of Fe3O4@ chitosan@ ZIF-8 towards removal of malachite green from aqueous solution: Theoretical and experimental studies, Int. J. Biol. Macromol. 168 (2021) 428–441.
[8] R. Ma, W. Fang, H. Zhang, J. Sun, H. Su, T. Chen, K. Hu, Transcriptome analysis of zebra fish (Danio rerio) eggs following treatment with malachite green, Aquaculture 514 (2020) 734500.
[9] R. Thiruchelvi, R. Venkataraghavan, D. Sharmila, Optimization of environmental parameters by Plackett-Burman design and response surface methodology for the adsorption of Malachite green onto Gracilaria edulis, Mater. Today Proc. 37 (2021) 1859–1864.
[10] M.A. Adebayo, J.I. Adebomi, T.O. Abe, F.I. Areo, Removal of aqueous Congo red and malachite green using ackee apple seed–bentonite composite, Colloid Interface Sci. Commun. 38 (2020) 100311.
[11] J. Yadav, O. Sahu, Malachite green dye purification from effluent using synthesized ceramic clay: Characterisation; optimization and scale up, Ceram. Int. 49 (15) (2023) 24831–24851.
[12] N. Nasuha, S. Ismail, B. Hameed, Activated electric arc furnace slag as an effective and reusable Fenton-like catalyst for the photodegradation of methylene blue and acid blue 29, J. Environ. Manag. 196 (2017) 323–329.
[13] M.E. Awad, A.M. Farrag, A.A. El-Bindary, M.A. El-Bindary, H.A. Kiwaan, Photocatalytic degradation of rhodamine B dye using low-cost pyrofabricated titanium dioxide quantum dots-kaolinite nanocomposite, Appl. Organomet. Chem. 37 (7) (2023) e7113.
[14] M.E. Awad, A.M. Farrag, M.M. Aboelnga, A.A. El-Bindary, Optimization of Photocatalytic Degradation of Rhodamine B and Indigo Carmine Dyes Using Eco-Friendly Kaolinite-Silver Oxide Quantum Dots Nanocomposite Under Sunlight Irradiation, Appl. Organomet. Chem. 39 (2) (2025) e7842.
[15] A. Hosseini, J. Foroughi, M.M. Sabzehmeidani, M. Ghaedi, Heterogeneous photoelectro-Fenton using ZnO and TiO2 thin film as photocatalyst for photocatalytic degradation Malachite Green, Appl. Surf. Sci. Adv. 6 (2021) 100126.
[16] N.M. Danesh, P. Lavaee, M. Ramezani, M. Alibolandi, M. Kianfar, M.A. Nameghi, K. Abnous, S.M. Taghdisi, An electrochemical sensing method based on an oligonucleotide structure for ultrasensitive detection of malachite green, Microchem. J. 160 (2021) 105598.
[17] A.P. Shah, S. Jain, V.J. Mokale, N.G. Shimpi, High performance visible light photocatalysis of electrospun PAN/ZnO hybrid nanofibers, J. Ind. Eng. Chem. 77 (2019) 154–163.
[18] S. Varjani, P. Rakholiya, H.Y. Ng, S. You, J.A. Teixeira, Microbial degradation of dyes: An overview, Bioresour. Technol. 314 (2020) 123728.
[19] T. Thejaswini, D. Prabhakaran, M.A. Maheswari, Ultrasound assisted synthesis of nano-rod embedded petal designed α-Bi2O3-ZnO nanoparticles and their ultra-responsive visible light induced photocatalytic properties, J. Photochem. Photobiol. A Chem. 335 (2017) 217–229.
[20] C. Byrne, G. Subramanian, S.C. Pillai, Recent advances in photocatalysis for environmental applications, J. Environ. Chem. Eng. 6 (3) (2018) 3531–3555.
[21] C. Hitam, A. Jalil, A review on exploration of Fe2O3 photocatalyst towards degradation of dyes and organic contaminants, J. Environ. Manag. 258 (2020) 110050.
[22] J. Das, V.S. Moholkar, S. Chakma, Structural, magnetic and optical properties of sonochemically synthesized Zr-ferrite nanoparticles, Powder Technol. 328 (2018) 1–6.
[23] P. Dhiman, A. Kumar, G. Rana, G. Sharma, Cobalt–zinc nanoferrite for synergistic photocatalytic and peroxymonosulfate-assisted degradation of sulfosalicylic acid, J. Mater. Sci. 58 (24) (2023) 9938–9966.
[24] P. Dhiman, T. Mehta, A. Kumar, G. Sharma, M. Naushad, T. Ahamad, G.T. Mola, Mg0. 5NixZn0. 5-xFe2O4 spinel as a sustainable magnetic nano-photocatalyst with dopant driven band shifting and reduced recombination for visible and solar degradation of Reactive Blue-19, Adv. Powder Technol. 31 (12) (2020) 4585–4597.
[25] A. Adewuyi, O.A. Ogunkunle, R.A. Oderinde, Zirconium ferrite incorporated zeolitic imidazolate framework-8: a suitable photocatalyst for degradation of dopamine and sulfamethoxazole in aqueous solution, RSC Adv. 13 (14) (2023) 9563–9575.
[26] S.R. Ali, A. Kalam, A.G. Al-Sehemi, Z. Khan, S. Ansari, N. Haider, R. Kumar, Zirconium-Ferrite Nanoparticles As Improved Adsorbent for Co 2+, Cu 2+, and Zn 2+: Thermodynamic and Kinetic Studies, Russ. J. Phys. Chem. A 94 (2020) 2797–2809.
[27] A. Bassi, I. Hasan, K. Qanungo, B.H. Koo, R.A. Khan, Visible light assisted mineralization of malachite green dye by green synthesized xanthan gum/agar@ ZnO bionanocomposite, J. Mol. Struct. 1256 (2022) 132518.
[28] C. Duan, C. Liu, X. Meng, K. Gao, W. Lu, Y. Zhang, L. Dai, W. Zhao, C. Xiong, W. Wang, Facile synthesis of Ag NPs@ MIL-100 (Fe)/guar gum hybrid hydrogel as a versatile photocatalyst for wastewater remediation: Photocatalytic degradation, water/oil separation and bacterial inactivation, Carbohydr. Polym. 230 (2020) 115642.
[29] A.M. Hasan, M.E. Abdel-Raouf, Applications of guar gum and its derivatives in petroleum industry: A review, Egypt. J. Pet. 27 (4) (2018) 1043–1050.
[30] R. Ramya, D. Nathiya, P. Thivya, J. Wilson, Functionally anchored Ag-TiO2 nanoparticles on guar gum based nanocomposite for simultaneous determination of hydroquinone, catechol, resorcinol and nitrite, Microchem. J. 170 (2021) 106734.
[31] L. Chopra, A. Sharma, J.S. Chohan, V.V. Upadhyay, R. Singh, S. Sharma, S. P. Dwivedi, A. Kumar, E.M. Tag-Eldin, Synthesis and characterizations of super

adsorbent hydrogel based on biopolymer, Guar Gum-grafted-Poly (hydroxyethyl methacrylate)(Gg-g-Poly (HEMA)) for the removal of Bismarck brown Y dye from aqueous solution, Int. J. Biol. Macromol. 256 (2024) 128518.
[32] P. Malik, M. Srivastava, R. Verma, M. Kumar, D. Kumar, J. Singh, Nanostructured SnO2 encapsulated guar-gum hybrid nanocomposites for electrocatalytic determination of hydrazine, Mater. Sci. Eng. C 58 (2016) 432–441.
[33] I. Pal, L. Chopra, S. Rajendran, P. Lalitha, K. Pal, N. Asthana, M.G. Paraje, Novel synthesis of GG-g-PAN based hydrolyzed products exclusion of congo red and methylene blue dyes undertaken aqueous medium for spectroscopic investigations, J. Mol. Liq. 416 (2024) 126346.
[34] D. Pathania, R. Katwal, G. Sharma, M. Naushad, M.R. Khan, A.a.H. Al-Muhtaseb, Novel guar gum/Al2O3 nanocomposite as an effective photocatalyst for the degradation of malachite green dye, Int. J. Biol. Macromol. 87 (2016) 366–374.
[35] R. Tabatabaeian, M. Dinari, H.M. Aliabadi, Cross-linked bionanocomposites of hydrolyzed guar gum/magnetic layered double hydroxide as an effective sorbent for methylene blue removal, Carbohydr. Polym. 257 (2021) 117628.
[36] J. Balachandramohan, R. Singh, T. Sivasankar, S. Manickam, Sonochemical synthesis of highly efficient Ag3PO4-Guar gum nanocomposite with photo-oxidation property under visible light irradiation, Chemical Engineering and Processing-Process Intensification 168 (2021) 108549.
[37] N. Mohammad Hosseini, S. Sheshmani, A.S. Shahvelayati, Manganese ferrite-graphite oxide-chitosan nanocomposite for efficient dye removal from aqueous and textile wastewater under UV and sunlight irradiation, Sci. Rep. 15 (1) (2025) 866.
[38] M. Rani, S. Sharma, A. Yadav, U. Shanker, Synergistic photocatalytic and adsorptive removal of organic dyes using ZnO–Fe2O3 nanoparticles incorporated into guar gum-carboxymethyl cellulose biopolymer matrix, Int. J. Biol. Macromol. 335 (2025) 149212.
[39] V. Karthik, G. Dhivya Dharshini, P. Senthil Kumar, S. Kiruthika, G. Rangasamy, S. Periyasamy, B. Senthil Rathi, Ferrite-supported nanocomposite polymers for emerging organic and inorganic pollutants removal from wastewater: A review, Ind. Eng. Chem. Res. 62 (35) (2023) 13711–13733.
[40] B. Alqassem, F. Banat, G. Palmisano, M.A. Haija, Emerging trends of ferrite-based nanomaterials as photocatalysts for environmental remediation: A review and synthetic perspective, Sustain. Mater. Technol. 40 (2024) e00961.
[41] R.S. Dassanayake, S. Acharya, N. Abidi, Recent advances in biopolymer-based dye removal technologies, Molecules 26 (15) (2021) 4697.
[42] A.S. Al-Wasidi, E.A. Abdelrahman, K.u. Rehman, F.A. Saad, A.M. Munshi, Efficient removal of crystal violet and acid red 88 dyes from aqueous environments using easily synthesized copper ferrite nanoparticles, Sci. Rep. 14 (1) (2024) 29599.
[43] S. Kundu, M.F. Abdullah, A. Das, A. Basu, A. Halder, M. Das, A. Samanta, A. Mukherjee, Antifungal ouzo nanoparticles from guar gum propionate, RSC Adv. 6 (108) (2016) 106563–106571.
[44] M.J. Saadh, H.E.N. Khasawneh, G.G.R. Ortiz, M. Ahsan, D.K. Sain, K. Yusuf, M. Sillanää, A. Iqbal, R. Akhavan-Sigari, Author Correction: Synthesis and characterization of ZrFe2O4@ SiO2@ Ade-Pd as a novel, recyclable, green, and versatile catalyst for Buchwald–Hartwig and Suzuki–Miyaura cross-coupling reactions. Sci. Rep. 14 (2024) 7839.
[45] N. Kaur, A. Katoch, S. Singh, R. Kaur, Properties of zirconium ferrite nanoparticles prepared by hydrothermal process, Mater. Lett. 330 (2023) 133236.
[46] S. Kavitha, M. Kurian, Effect of zirconium doping in the microstructure, magnetic and dielectric properties of cobalt ferrite nanoparticles, J. Alloys Compd. 799 (2019) 147–159.
[47] Y. Xia, Z. He, J. Su, B. Tang, K. Hu, Y. Lu, S. Sun, X. Li, Fabrication of magnetically separable NiFe 2 O 4/BiOI nanocomposites with enhanced photocatalytic performance under visible-light irradiation, RSC Adv. 8 (8) (2018) 4284–4294.
[48] I. Hasan, A. Bassi, P. Kalakonda, CuO surface functionalized β-cyclodextrin grafted PMMA hybrid nanocomposite for advance oxidative mineralization of methyl orange, Surf. Interfaces 56 (2025) 105456.
[49] S.R. Teeparthi, E.W. Awin, R. Kumar, Dominating role of crystal structure over defect chemistry in black and white zirconia on visible light photocatalytic activity, Sci. Rep. 8 (1) (2018) 5541.
[50] L. Li, P. Ma, S. Hussain, L. Jia, D. Lin, X. Yin, Y. Lin, Z. Cheng, L. Wang, FeS 2/carbon hybrids on carbon cloth: a highly efficient and stable counter electrode for dye-sensitized solar cells, Sustainable Energy Fuels 3 (7) (2019) 1749–1756.
[51] P. Bargiela, V. Fernandez, C. Cardinaud, J. Walton, M. Greiner, D. Morgan, N. Fairley, J. Baltrusaitis, Towards a reliable assessment of charging effects during surface analysis: Accurate spectral shapes of ZrO2 and Pd/ZrO2 via X-ray Photoelectron Spectroscopy, Appl. Surf. Sci. 566 (2021) 150728.
[52] S. Wu, W. Xiong, H. Li, Insights into the Fe oxidation state of sphere-like Fe2O3 nanoparticles for simultaneous Pb2+ and Cu2+ detection, J. Alloys Compd. 934 (2023) 167863.
[53] A. Bassi, P. Kalakonda, I. Hasan, Synthesis of Chitosan-Agar immobilized NiO-MgO bionanocomposites and their photocatalytic application towards toxic azo dye, Inorg. Chem. Commun. 170 (2024) 113499.
[54] S. Huang, C. Chen, H. Tsai, J. Shaya, C. Lu, Photocatalytic degradation of thiobencarb by a visible light-driven MoS2 photocatalyst, Sep. Purif. Technol. 197 (2018) 147–155.
[55] J.T. Schneider, D.S. Firak, R.R. Ribeiro, P. Peralta-Zamora, Use of scavenger agents in heterogeneous photocatalysis: Truths, half-truths, and misinterpretations, Phys. Chem. Chem. Phys. 22 (27) (2020) 15723–15733.
[56] X. Zheng, J. Yuan, J. Shen, J. Liang, J. Che, B. Tang, G. He, H. Chen, A carnation-like rGO/Bi2O2CO3/BiOCl composite: efficient photocatalyst for the degradation of ciprofloxacin, J. Mater. Sci. Mater. Electron. 30 (6) (2019) 5986–5994.
[57] L. Wang, H. Zhai, G. Jin, X. Li, C. Dong, H. Zhang, B. Yang, H. Xie, H. Sun, 3D porous ZnO–SnS p–n heterojunction for visible light driven photocatalysis, Phys. Chem. Chem. Phys. 19 (25) (2017) 16576–16585.
[58] I. Hasan, F.A. Alharthi, Caffeine-alginate immobilized CeTiO4 bionanocomposite for efficient photocatalytic degradation of methylene blue, J. Photochem. Photobiol. A Chem. 433 (2022) 114126.
[59] Y. Chi, W. Wang, Q. Zhang, H. Yu, M. Liu, S. Ni, B. Gao, S. Xu, Evaluation of practical application potential of a photocatalyst: ultimate apparent photocatalytic activity, Chemosphere 285 (2021) 131323.
[60] A.N. Che Abdul Rahim, S. Yamada, H. Bonkohara, S. Mestre, T. Imai, Y.-T. Hung, I. Kumakiri, Influence of salts on the photocatalytic degradation of formic acid in wastewater, Int. J. Environ. Res. Public Health 19 (23) (2022) 15736.
[61] S. Liu, P.C. Edara, A.I. Schäfer, Influence of organic matter on the photocatalytic degradation of steroid hormones by TiO2-coated polyethersulfone microfiltration membrane, Water Res. 245 (2023) 120438.
[62] S. Jabeen, A.S. Ganie, S. Bala, T. Khan, Photocatalytic degradation of malachite green dye via an inner transition metal oxide-based nanostructure fabricated through a hydrothermal route, Materials Proceedings 14 (1) (2023) 5.
[63] A. Hassani, P. Eghbali, A. Ekicibil, Ö. Metin, Monodisperse cobalt ferrite nanoparticles assembled on mesoporous graphitic carbon nitride (CoFe2O4/mpg-C3N4): A magnetically recoverable nanocomposite for the photocatalytic degradation of organic dyes, J. Magn. Magn. Mater. 456 (2018) 400–412.
[64] Z.H. Jaffari, S.-M. Lam, J.-C. Sin, H. Zeng, Boosting visible light photocatalytic and antibacterial performance by decoration of silver on magnetic spindle-like bismuth ferrite, Mater. Sci. Semicond. Process. 101 (2019) 103–115.
[65] G. Meenakshi, B. Manjunath, S. Prashantha, T. Prashanth, B. Surendra, Super capacitor, electrochemical measurement and sun light driven photocatalytic applications of CuFe2O4 NPs synthesized from bio-resource extract, Sensors International 4 (2023) 100237.
[66] S. Bibi, A. Ahmad, M.A.R. Anjum, A. Haleem, M. Siddiq, S.S. Shah, A. Al Kahtani, Photocatalytic degradation of malachite green and methylene blue over reduced graphene oxide (rGO) based metal oxides (rGO-Fe3O4/TiO2) nanocomposite under UV-visible light irradiation, J. Environ. Chem. Eng. 9 (4) (2021) 105580.
[67] N. Arsalani, S. Bazazi, M. Abuali, S. Jodeyri, A new method for preparing ZnO/CNT nanocomposites with enhanced photocatalytic degradation of malachite green under visible light, J. Photochem. Photobiol. A Chem. 389 (2020) 112207.
[68] D.R. Rout, S. Chaurasia, H.M. Jena, Enhanced photocatalytic degradation of malachite green using manganese oxide doped graphene oxide/zinc oxide (GO-ZnO/Mn2O3) ternary composite under sunlight irradiation, J. Environ. Manag. 318 (2022) 115449.